

Research Article

Blasting-Induced Permeability Enhancement of Ore Deposits Associated with Low-Permeability Weakly Weathered Granites Based on the Split Hopkinson Pressure Bar

Lei Yan,¹ Wenhua Yi,¹ Liansheng Liu ^{1,2} Jiangchao Liu,³ and Shenghui Zhang¹

¹School of Resource and Environmental Engineering, Jiangxi University of Science and Technology, Ganzhou, 341000 Jiangxi, China

²Jiangxi Key Laboratory of Mining Engineering, Ganzhou, 341000 Jiangxi, China

³College of Architecture and Civil Engineering, Beijing University of Technology, Beijing 100022, China

Correspondence should be addressed to Liansheng Liu; liulsjxust@163.com

Received 5 July 2018; Accepted 30 September 2018; Published 23 December 2018

Guest Editor: Fangtian Wang

Copyright © 2018 Lei Yan et al. This is an open access article distributed under the Creative Commons Attribution License, which permits unrestricted use, distribution, and reproduction in any medium, provided the original work is properly cited.

By utilizing the improved split Hopkinson pressure bar (SHPB) test device, uniaxial, constant-speed cyclic, and variable-speed cyclic impact compression tests were conducted on weakly weathered granite samples. By combining nuclear magnetic resonance (NMR) and triaxial seepage tests, this study investigated the change laws in the mechanical properties, porosity evolution, and permeability coefficients of the samples under cyclic impacts. The results showed that in constant-speed cyclic impacts with increasing impact times, deformation modulus decreased, whilst porosity firstly decreased and then increased. Furthermore, dynamic peak strength firstly increased and then decreased whereas peak strain constantly increased before failure of the samples. In the variable-speed cyclic impacts, as impact times increased, deformation modulus firstly increased and then declined with damage occurring after four impact times. The compaction process weakened and even disappeared with increasing initial porosity. Three types of pores were found in the samples that changed in multiscale under cyclic loading. In general, small pores extended to medium- and large-sized pores. After three variable-speed cyclic impacts, the porosity of the samples was larger than the initial porosity and the permeability coefficient was greater than its initial value. The results demonstrate that the purpose of enhancing permeability and keeping the ore body stable can be achieved by conducting three variable-speed cyclic impacts on the samples.

1. Introduction

In situ leach mining has numerous advantages as it is a relatively simple process and is low-cost and environment-friendly. It is an approach that is widely used to extract or recover low-grade ore bodies, such as uranium, copper, gold, and ion-adsorbed rare earth minerals that are difficult to recover using conventional mining methods [1]. However, the promotion of *in situ* leach mining in ion-adsorbed rare earth ores is mainly limited by the permeability of ore bodies [2]. Due to many prominent contradictions of rare earth deposits that are associated with low-permeability weathered granites in an *in situ* leach mining process [3], the development and utilization of ion-adsorbed rare earth ores are

significantly restricted. By referring to the permeability enhancement methods proposed for *in situ* leach mining of low-permeability oil and gas fields, coalbed methane (CBM), and sandstone-type uranium deposits [4–8], the central concept of “blasting with small dosages and precisely controlled time delay” in rare earth ore bodies has been proposed. In this process, blasting stress waves are used to generate multiple dynamic disturbances on the rare earth ore bodies and change the internal mesostructure, thus enhancing permeability and maintaining ore body stability. Blasting and permeability enhancement of ore deposits associated with low-permeability weakly weathered granites are a rapid, complex, and continuous process. The essence is the accumulation of internal damage of rocks under multiple

disturbances of blasting stress waves, which is shown as the expansion and connection of mesocracks and enhancement of macropermeability.

Zhang and Zhao [9] summarized dynamic testing technologies for rock materials, which provides references for carrying out laboratory tests on blasting-induced permeability enhancement. Damage evolution of rock internal defects under dynamic disturbance was of great significance to its permeability, and there were plenty of theoretical achievements in this field. Using nuclear magnetic resonance (NMR) technology, Zhou et al. [10] studied the evolution process of microscopic damage of rocks under freeze-thaw cycles and analyzed the influences of freeze-thaw cycle times and porosity on dynamic and static mechanical properties. Based on the split Hopkinson pressure bar (SHPB) test, Xia et al. [11] researched the effects of microstructures on deformation characteristics and failure modes of Barre granite (BG). Wang et al. [12, 13] studied the mechanical properties and mesofracture evolution of coal samples with different water contents under static and dynamic loads and dynamic and static combined loads. Gong et al. [14, 15] studied the mechanical properties of rock under one-dimensional and three-dimensional dynamic and static combination and the law of internal crack propagation. Li et al. [16] investigated the dynamic characteristics of granites under impact loads, obtaining the change laws of stress-strain curves under cyclic impacts. Through uniaxial cyclic impact loading on granites by carrying out SHPB, Zhu et al. [17] revealed the damage laws and mechanisms of multiple blasting on rock masses in engineering construction. Based on a triaxial seepage test, Liu et al. [18] investigated the evolution of permeability in sandstones with and without mud under different loading conditions and analyzed the factors influencing permeability changes. Based on studies on the permeability of ion-adsorbed rare earth ores by combining with hydrodynamics, Tian et al. [19] obtained that porosity is positively correlated with permeability. It is therefore of great significance to investigate blasting-induced permeability enhancement to gain further understanding of pore structure, pore distribution, and damage evolution under cyclic impact of weakly weathered granites.

Taking weakly weathered granites as research objects, this study conducted uniaxial, constant-speed cyclic, and variable-speed cyclic impact compression tests using the improved SHPB device [20]. The evolution laws of pore damage have been studied using NMR technology. Furthermore, by conducting triaxial seepage tests with the GDS-VIS device, the permeability coefficients before and after impacts were determined. This provides a theoretical basis and engineering guidance for correctly understanding blasting and permeability enhancement mechanisms of ore deposits associated with low-permeability weakly weathered granites and for scientifically designing optimal blasting parameters.

2. Experiment

2.1. Specimen Preparation. Samples of weakly weathered granites were obtained from weakly weathered strata (with a burial depth of 10 m) in a rare earth mine in Anyuan



FIGURE 1: Processed weakly weathered granite specimens [23]. “The figure is reproduced from Yan et al. [23] (under the Creative Commons Attribution License/public domain).”

County (Southern Jiangxi Province, China). The samples were coarse biotite granites formed in the early Yanshanian Period (from Jurassic to early Cretaceous) and comprised feldspar, quartz, biotite, and a small amount of clay minerals. According to guidelines from the International Society for Rock Mechanics (ISRM), the blanks of rock samples were processed in the laboratory into cylinder samples with a diameter of 50 mm. For samples in static load tests (including uniaxial compression test and indirect tensile test), they were prepared in accordance with length-to-diameter ratios being 2 and 0.5. In the uniaxial impact compression test, the samples were prepared with a length-to-diameter ratio of 1. By studying size effects of brittle materials such as rocks under impact loads, Dai et al. [21] found that a length-to-diameter ratio ranging between 0.5 and 2 had slight influences on test results. Research conducted by Zhou et al. [22] showed that length-to-diameter ratios of 0.5 and 1 were feasible. In the dynamic and static loading tests, the nonparallelism and nonperpendicularity of the end faces of the samples were less than 0.02 mm. Figure 1 shows some processed samples. To avoid the impacts of moisture on test results, all processed samples were dried for 24 h in the 101-1 electrothermal oven blowing constant temperature at 108°C and then put into dryers for cooling to room temperature. The longitudinal wave velocity v_p was tested using an RSM-SY5 intelligent acoustic detector.

The basic mechanical performance test was conducted on dried samples of weakly weathered granites using an RMT-150 C test machine produced by the Key Laboratory of Mining Projects in Jiangxi Province, China. The physical and mechanical parameters are shown in Table 1. Figure 2 demonstrates the failure modes of rock samples in the static load test. The Carr-Purcell-Meiboom-Gill (CPMG) pulse sequence test was carried out, and n_q was calculated after performing dry/wet vacuum saturated water treatment on samples using an NM-60 NMR analyzer manufactured by Shanghai Niumag Electronic Technology Co. Ltd., which was combined with vacuum saturation devices. The basic

TABLE 1: Physicomechanical parameters of weakly weathered granites.

ρ (kg·m ⁻³)	$\dot{\epsilon}$ (s ⁻¹)	σ_{qc} (MPa)	σ_{qt} (MPa)	E (GPa)	μ
2312	1.0×10^{-7}	28.164	4.71	7.821	0.281

Remarks: ρ is the density, $\dot{\epsilon}$ is the strain rate, σ_{qc} is the quasi-static compressive strength, σ_{qt} is the quasi-static tensile strength, E is the elastic modulus, and μ is Poisson's ratio.

principle of NMR core measurement is available from previously published studies [24, 25].

2.2. Test Devices and Principle

2.2.1. Uniaxial Impact Compression Test. The impact test was performed using the dynamic and static combined loading test system [20] in Jiangxi University of Science and Technology (Ganzhou City, China). Figure 3 displays the SHPB test system with a diameter of 50.00 mm. The striker and bars of the device were made of 40 Cr alloy steel with a density of 7810 kg/m³ and a longitudinal wave velocity of 5400 m/s. The elastic limit and wave impedance were 800 MPa and 42 TPa/s, respectively. In addition, the lengths of the incident, transmitted, and absorption bars were 2.0 m, 1.5 m, and 0.5 m, respectively. P-C vibration could be eliminated by the cone-shaped striker, thus realizing a loading at a constant strain rate. The diameter and length of the striker were 50.00 mm and 360.10 mm, respectively [26–29].

In the impact tests, the incident strain $\epsilon_I(t)$, reflected strain $\epsilon_R(t)$, and transmitted strain $\epsilon_T(t)$ could be indirectly calculated measuring voltages of resistance strain gauges pasted on the incident bar and transmitted bar. Based on one-dimensional stress wave theory, the strain rate $\dot{\epsilon}_{dc}(t)$, strain $\epsilon_{dc}(t)$, and stress $\sigma_{dc}(t)$ of brittle, weakly weathered granites were accurately calculated using the three-wave method [9, 30, 31]. The expressions are shown as

$$\sigma_{dc}(t) = \frac{A_e E_e}{2A} [\epsilon_I(t) + \epsilon_R(t) + \epsilon_T(t)], \quad (1)$$

$$\epsilon_{dc}(t) = -\frac{c_e}{L} \int_0^t [\epsilon_I(t) + \epsilon_R(t) - \epsilon_T(t)] dt, \quad (2)$$

$$\dot{\epsilon}_{dc}(t) = -\frac{c_e}{L} [\dot{\epsilon}_I(t) + \dot{\epsilon}_R(t) - \dot{\epsilon}_T(t)], \quad (3)$$

where A and L indicate the cross-sectional area and length of the samples separately. E_e and A_e represent the elastic modulus and the cross-sectional area of the pressure bar, respectively. c_e denotes the longitudinal wave velocity of the pressure bar and $c_e = \sqrt{E_e/\rho_e}$, where ρ_e and τ show the material density of the pressure bar and the duration of stress waves, respectively.

2.2.2. Triaxial Seepage Test. The test was completed using the GDS-VIS400kN HPTAS high-pressure temperature-controlled triaxial rheometer for rocks produced by the GDS Company, United Kingdom. Equipped with the virtual infinite stiffness load frame (VIS) developed by the GDS Company, this system had a GDS feedback control system

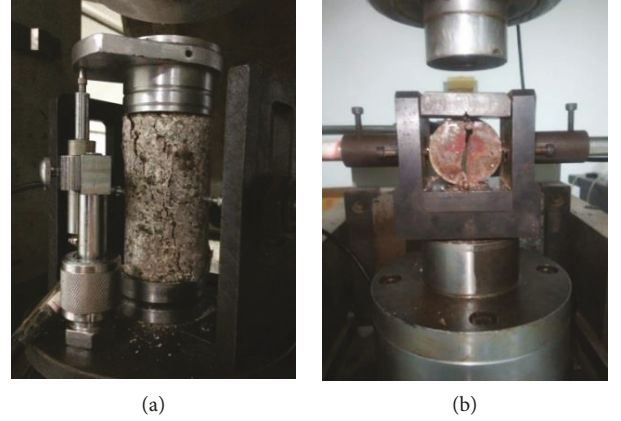


FIGURE 2: Failure modes of rock specimens under static loads: (a) the uniaxial compression failure with (b) the indirect tensile failure.

and matched GDSLAB software. The system could be used to conduct uniaxial and triaxial compression tests, rheological testing of the rocks, and seepage-stress coupling test. The axial, confining, and seepage pressures were applied utilizing three independent systems. The test parameters were set on the computer and operated through the manual controller. The maximum axial load was 400 kN. The confining pressure ranged from 0 to 32 MPa, and the pore water pressure varied from 0 to 32 MPa. The test system is shown in Figure 4.

Using the steady-state method, the permeability test was performed on weakly weathered granite samples before and after impacts, that is, the osmotic pressure difference formed in the two ends of the rock samples, to record the inflow volume V of seepage water, lateral confining pressure, and osmotic pressure difference. The expression is [18, 32]

$$k = \frac{\mu L Q}{A \Delta p}, \quad (4)$$

where Q indicates the flow of fluids passing through rocks per unit time (cm³/s). A represents the cross-sectional area of fluids flowing through rocks (cm²). μ shows the viscosity of fluids (1.0×10^{-3} Pa·s of water at 20°C). L denotes the length of rocks (cm). Δp and k demonstrate the pressure difference before and after fluids flowing through the rocks (MPa) and the permeability coefficient of rocks, respectively.

2.3. Testing Procedure. The test process was as follows:

- (1) Rock samples were processed into standard cylinders required in the test, and longitudinal wave velocities of each sample were tested, to minimize inconsistent weathering of samples. The uniaxial compression and indirect tensile tests were conducted on the samples to obtain basic mechanical parameters
- (2) The NMR test was conducted on the samples that had undergone the uniaxial impact compression test to measure porosity and characterize the T_2 spectrum distribution of the pore structures. Moreover,

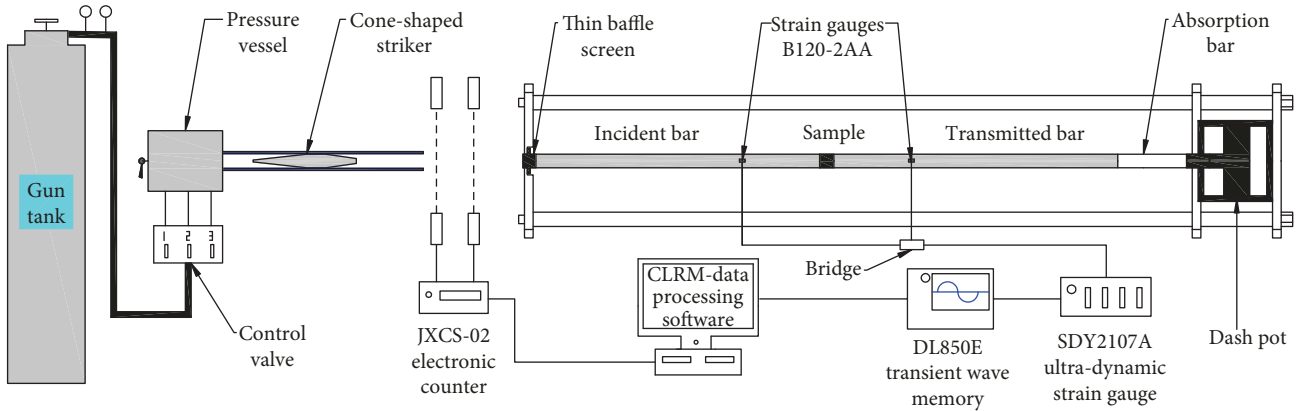


FIGURE 3: The SHPB test system.

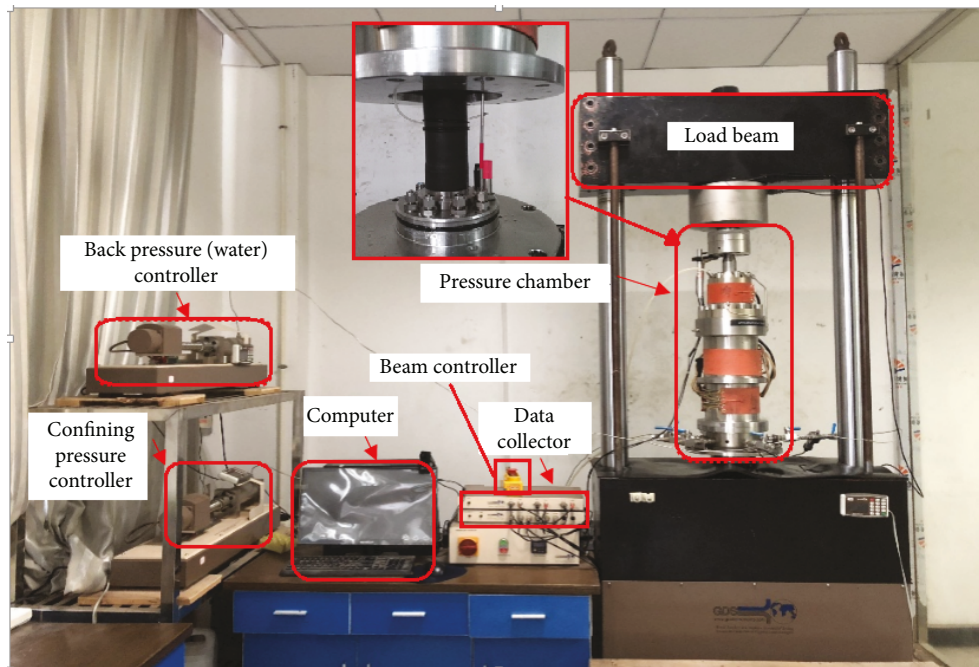


FIGURE 4: GDS-VIS triaxial rheometer.

the samples were uniformly divided into three groups, i.e., M group (single impact group at different impact velocities), N group (constant-speed cyclic impact to crack), and O group (variable-speed cyclic impact to crack)

- (3) Impact tests were conducted on the M, N, and O groups. Before the impact test, the stress balance at both ends of the rock sample was checked to ensure the accuracy of the obtained test data [33]. Since the depth of the sample was shallow, the influence of axial pressure and confining pressure on the experimental results was not considered. In the tests, the contact surfaces of the samples and bars were uniformly smeared with lubricating oil to reduce friction effects on the end faces [21]. The impact velocity of the striker was controlled by adjusting the impact pressures and positions of the striker in the emission

cavity. Single impact tests were conducted on the M group at velocities of about 4.0, 5.0, 6.0, 7.0, and 8.0 m/s, to determine the threshold value of cyclic impact loads [16]. Constant-speed cyclic impact tests were conducted at velocities of 4.0, 5.0, and 6.0 m/s. Variable-speed tests were performed at 4.1, 5.3, 6.3, and 7.0 m/s. On this basis, pore evolution laws of weakly weathered granites under multiple impact loads were investigated and effective porosity was characterized

- (4) This study carried out triaxial seepage tests on the samples with porosity ranging from 2% to 5% in the O group before impacts and after three impacts. Permeability coefficients were determined before and after impacts. According to the reference values of pore water pressure in the in situ leach mining of rare earth mines, the pore water pressure at the water inlet

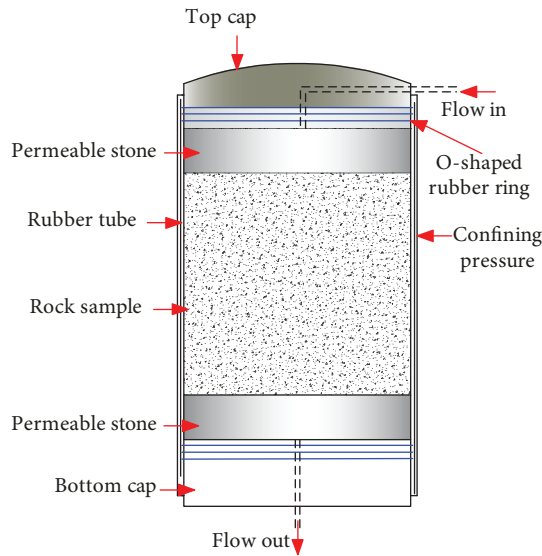


FIGURE 5: Schematic diagram of rock sample installation.

was kept unchanged at 0.6 MPa, whilst that at the water outlet was atmospheric pressure. Moreover, the confining pressure was larger than the seepage pressure and set to 2 MPa. In the seepage test, the influence of burial depth on permeability coefficients was large and therefore could not be ignored, so 0.25 MPa of the axial load was applied. Specific operations of the seepage tests are given in the literature [18, 32], and installation of the samples is shown in Figure 5

3. Results and Discussion

3.1. Determination of the Threshold Value of Cyclic Impact Velocity. Weakly weathered granite samples with porosity ranging from 1.5% to 7% were used to determine the threshold value of cyclic impact loads. The influences of impact velocity of the striker and initial porosity on dynamic peak strength were also determined [34]. In accordance with a previous study [16], only when the dynamic peak strength was larger than 80% of the uniaxial compressive strength can effective damages be generated in the rocks. For samples with a small porosity, the impact was conducted at a low velocity. If samples were damaged, it can be speculated that samples with a large porosity can also be damaged at the same impact velocity. If the dynamic peak strength of the samples is lower than 80% of the uniaxial compressive strength, the minimum impact velocity increased. Samples with a large porosity were impacted at a large velocity. If the samples were not damaged, the maximum impact velocity is accelerated. If they are damaged, samples with minimum porosity are impacted. When samples with minimum porosity are damaged, the maximum impact velocity was reduced. Using the above method, the upper and lower limits of impact velocity were determined and divided into control groups of single impact tests with different impact velocities according to constant gradients. Through multiple trial impacts, the test for determining threshold values of the cyclic impact loads was carried out

with impact velocity being approximately 4 m/s~8 m/s. The test results are displayed in Table 2. Rock samples subjected to impact at a velocity of about 4~6 m/s showed no obvious surface damage, and the dynamic peak strength is larger than 80% of the uniaxial compressive strength. Moreover, effective porosity changed significantly, indicating that effective damage was generated inside. When impact velocity was approximately 7 m/s, small cracks appeared on the side of the samples near to the incident bar in the axial direction and extended to the middle of the samples which did not connect, as shown in Figure 6(a). When impact velocity is approximately 8 m/s, splitting failure is shown in the axial direction of the samples, as demonstrated in Figure 6(b). Therefore, the cyclic impact velocity that caused effective damage ranged from 4 to 7 m/s.

Figure 7 shows the stress-strain curves of the samples at different impact velocities. By combining with Table 2, it can be seen that in the allowable value range of the test, when the increment of v was 1 m/s and change amplitude of n_q was less than 0.5%, the dynamic peak strength was controlled by v ; when the change amplitude of n_q was larger than 0.5%, the dynamic peak strength was mainly affected by n_q ; and when the increment of v was larger than 1 m/s, the dynamic peak strength was greatly influenced by v . Moreover, the strain rate was slightly affected by porosity, showing sensitivity to impact velocities. As shown in Figure 7, rebound of the stress-strain curve after the peak strength weakened but did not disappear with increased impact velocity which may be explained as follows. When the samples were not completely crushed but only had open cracks in local areas, stress waves could still be transmitted between the incident and the transmitted bar through the samples and rock samples that had certain bearing capacity. The stress-strain curves of each rock sample were basically the same in a bar-bell shape, and the initial tangent modulus overlapped. The deviation of M3 was large, which was because of its structure and distribution of internal initial defects. Strains of M4 and M5 corresponded to equal dynamic peak strength which was larger than those on the other curves. This indicated that there was a critical strain value (0.005) from plastic deformation to macroscopic failure of weakly weathered granites under single impacts.

3.2. Constant-Speed Cyclic Impact. The three groups of weakly weathered granite samples underwent constant-speed cyclic impact loading at impact velocities of 4, 5, and 6 m/s. Porosity was measured on the intact rock samples before and after each impact using the NMR device, and the test results are shown in Table 3. As demonstrated in the table, with increasing impact velocity, the impact times for samples to form macrocracks reduced significantly. The average strain rate in the first impact increased with impact velocity, and the dynamic peak strength was dispersed. This was influenced by many factors including impact velocity, initial defects, and the degree of weathering.

To study the dynamic characteristics of weakly weathered granites under constant-speed cyclic impacts, the strain signal waveforms, stress-strain curves, and failure modes

TABLE 2: Single impact at different impact speeds.

No.	v (m·s ⁻¹)	n_q (%)	L/D	ρ (g·cm ⁻³)	v_p (m·s ⁻¹)	σ_{dc} (MPa)	$\dot{\epsilon}_{dc}$ (s ⁻¹)	Observation
M1	4	3.929	1.032	2.249	1671	23.37	22.15	No damage
M2	5	3.755	1.026	2.253	1808	28.33	29.45	No damage
M3	6	4.026	1.038	2.161	1745	28.70	34.05	No damage
M4	7	4.545	1.031	2.258	1746	27.67	47.46	Damage
M5	8	6.806	1.053	2.226	1543	30.96	54.78	Damage

Remarks: v is the approximate impact velocity, n_q is the porosity, L/D is the slenderness ratio, ρ is the density, v_p is the longitudinal wave velocity, σ_{dc} is the dynamic compressive strengths, and $\dot{\epsilon}_{dc}$ is the average strain rate.

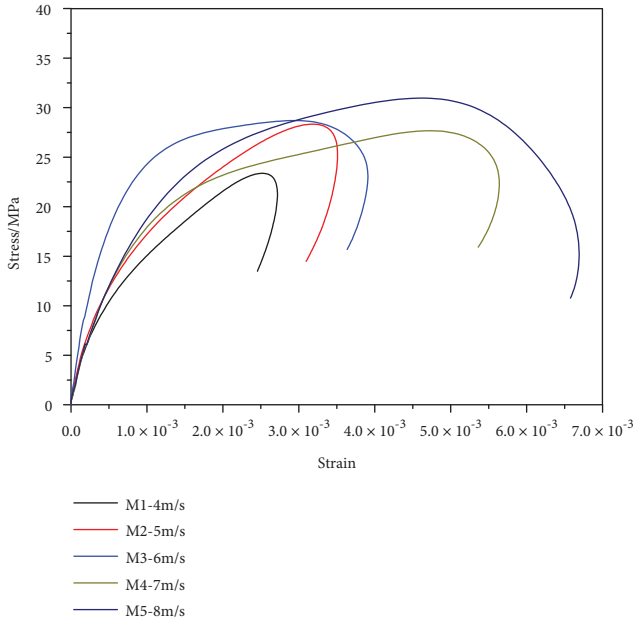
FIGURE 6: Single impact loading specimen failure mode: (a) M4 ($v = 7$ m/s) and (b) M5 ($v = 8$ m/s).

FIGURE 7: Stress-strain curves of specimens at different impact velocities.

of N-1-2, N-2-1, and N-3-3 were analyzed, as displayed in Figure 8.

As shown in Figure 8(a), with decreasing impact velocity, the amplitude of strain signal waveforms was reduced. Incident waves in each cyclic impact showed good reproducibility and were consistent. As impact times increased, the amplitude of the reflected waves increased because the number of pores in the samples increased after multiple impacts

and superimposed effects [35, 36] were generated from the multiple reflections of stress waves. After the cyclic impacts, the amplitude of transmitted waves reduced and waveforms increased more obviously. This was due to irreversible deformation in the rocks which constantly increased. In other words, at a certain incident energy, reflected energy and energy consumption of irreversible deformation increased [37], whilst transmitted energy decreased correspondingly. Different degrees of microelastic deformations existed whilst plastic deformation occurred in the samples. Elastic strain energy accumulated in the unloading was released in the form of a pulse and had effects on the transmitted bar causing a sudden jump of the transmitted waves.

In Figure 8(b), the dynamic peak strength decreased with reducing impact velocity and firstly showed an increase and then a decrease in change law with increasing impact times. Peak strain corresponding to dynamic peak strength increased with growing impact times on the whole. The peak strains reduced partially at the stage when the samples were about to be damaged and were minimal in the last impact. In the first impacts on the samples, internal pores and fissures were gradually compacted (Figure 9), raising the dynamic strength of rocks. In each impact, irreversible deformation occurred to the samples which gradually accumulated to constantly increased peak strain. When plastic deformation accumulated to a certain level, cracks in the sample subjected to the last impact rapidly connected to generate macrocracks and degrade mechanical performance. Under these conditions, peak strength could be reached under small deformation and stress levels but did not reduce to zero with increasing strain, indicating that the samples had certain bearing capacity. Before the samples were broken, the elasticity moduli of the stress-strain energy curves were

TABLE 3: Constant-velocity cyclic impact test data.

No.	v (m·s ⁻¹)	n_q (%)	$\frac{L}{D}$	ρ (g·cm ⁻³)	v_p (m·s ⁻¹)	σ_{dc} (MPa)	$\dot{\epsilon}_{dc}$ (s ⁻¹)	n
N-1-1	6	2.867	1.030	2.335	1794	29.78	37.97	6
N-1-2		3.220	1.032	2.295	1745	38.50	42.21	8
N-1-3		1.876	1.005	2.510	2083	43.89	39.82	7
N-1-4		2.854	1.021	2.328	1903	44.67	30.20	6
N-2-1	5	4.688	1.037	2.198	1663	36.26	24.70	9
N-2-2		2.173	1.020	2.392	1923	48.41	24.33	10
N-2-3		1.764	1.021	2.571	2113	57.50	27.92	14
N-2-4		3.604	1.029	2.296	1773	21.77	20.56	12
N-3-1	4	3.194	1.017	2.285	1879	31.76	19.46	15
N-3-2		1.834	1.030	2.428	1970	38.68	18.16	19
N-3-3		3.199	1.022	2.284	1842	36.80	16.50	16
N-3-4		3.359	1.037	2.288	1786	27.98	18.39	11

Remarks: v is the approximate impact velocity, n_q is the initial porosity, L/D is the slenderness ratio, ρ is the density, v_p is the longitudinal wave velocity, σ_{dc} is the first impact dynamic compressive strengths, $\dot{\epsilon}_{dc}$ is the first impact average strain rate, and n is the cumulative impact.

basically the same and the deformation moduli gradually reduced with increasing impact times. Some energy was consumed due to the expansion of initial cracks and the generation of new cracks under cyclic impact loads, which weakened load transfer capacity of the samples to further cause decreased deformation [17]. Failure modes of the samples under cyclic impacts (Figure 8(c)) were different from those under single impacts (Figure 6). Under cyclic impacts, small connected open cracks which were not parallel to loading direction appeared and showed small branches. Damage to the samples under cyclic dynamic disturbances belonged to damaged failure and was a progressive process. The failure mode was closely correlated with the generation, distribution, and expansion of internal cracks.

The above analyses found that the dynamic characteristics of weakly weathered granites under constant-speed cyclic impacts were greatly affected by mesostructure and the evolution process of mesostructure could be represented by porosity. Figure 9 shows the relationship between porosity of the samples subjected to impacts and different impact times.

It can be seen that porosity firstly decreased and then increased with impact times. The decrease in porosity during the compaction process was generally smaller than the increment of porosity in the growth process. Also, the larger the initial porosity, the more obvious the occurrence of the described changes. After the samples with similar initial porosity underwent cyclic impact loading, the porosities of each sample were approximate when fatigue damage occurred and impact times reduced with increasing impact velocity. By combining these data with the study of Deng et al. [38], irreversible deformation including generation of small-sized pores and compaction of large-sized pores took place in mesostructures of weakly weathered granite samples after experiencing each impact. During the compaction process, the volume of generated small-sized pores was smaller than that of the large-sized pores, which was shown as a reduction in porosity on the whole. In the growth process, small-sized pores further extended, nucleated, and connected

until failure of the samples occurred. In Section 3.3, further analysis was conducted based on transverse relaxation time T_2 spectra.

3.3. Variable-Speed Cyclic Impact. According to Sections 3.1 and 3.2, for ore deposits related to low-permeability weakly weathered granites, cyclic impact loading had more significant damaging effects and the increase in porosity of the samples could be controlled by cyclic times. In this way, samples were not damaged completely with increasing porosity and showed certain bearing capacity, to ensure stability of ore bodies in production. Using the blasting technique with precisely controlled time delay, the finite cyclic impact loads were applied on low-permeability ore bodies. When utilizing differential blasting technology, due to reflection, transmission, and superposition of blasting waves in different medium interfaces [39], impact loads acting on the objective ore bodies were difficult to reach due to the effects of constant-speed cyclic impacts. The mechanical properties and pore evolution characteristics of weakly weathered granites under variable-speed cyclic impacts should be considered. Figure 10 displays the stress-strain curves and transverse relaxation time T_2 spectra of three typical samples in the O group.

In Figure 10, the initial porosities of the three samples increased and the number of internal mesocracks rose successively. As shown in the stress-strain curves, the dynamic peak strength reduced and the peak strain increased after the first impact. When the impact velocity for each of the samples was approximate, the more the internal cracks, the larger the number of cracks that activated and extended during the loading process. These changes correspondingly increased the deformation and energy dissipation of deformation on the whole. Meanwhile, the load transfer capacity of the rocks weakened, thus reducing the dynamic peak strength. Under four impacts, the initial elasticity moduli of each sample were basically the same and the deformation moduli firstly increased and then decreased. The curve of the last impact was different from that of the constant-speed cyclic impact (the peak strain was larger than 0.005),

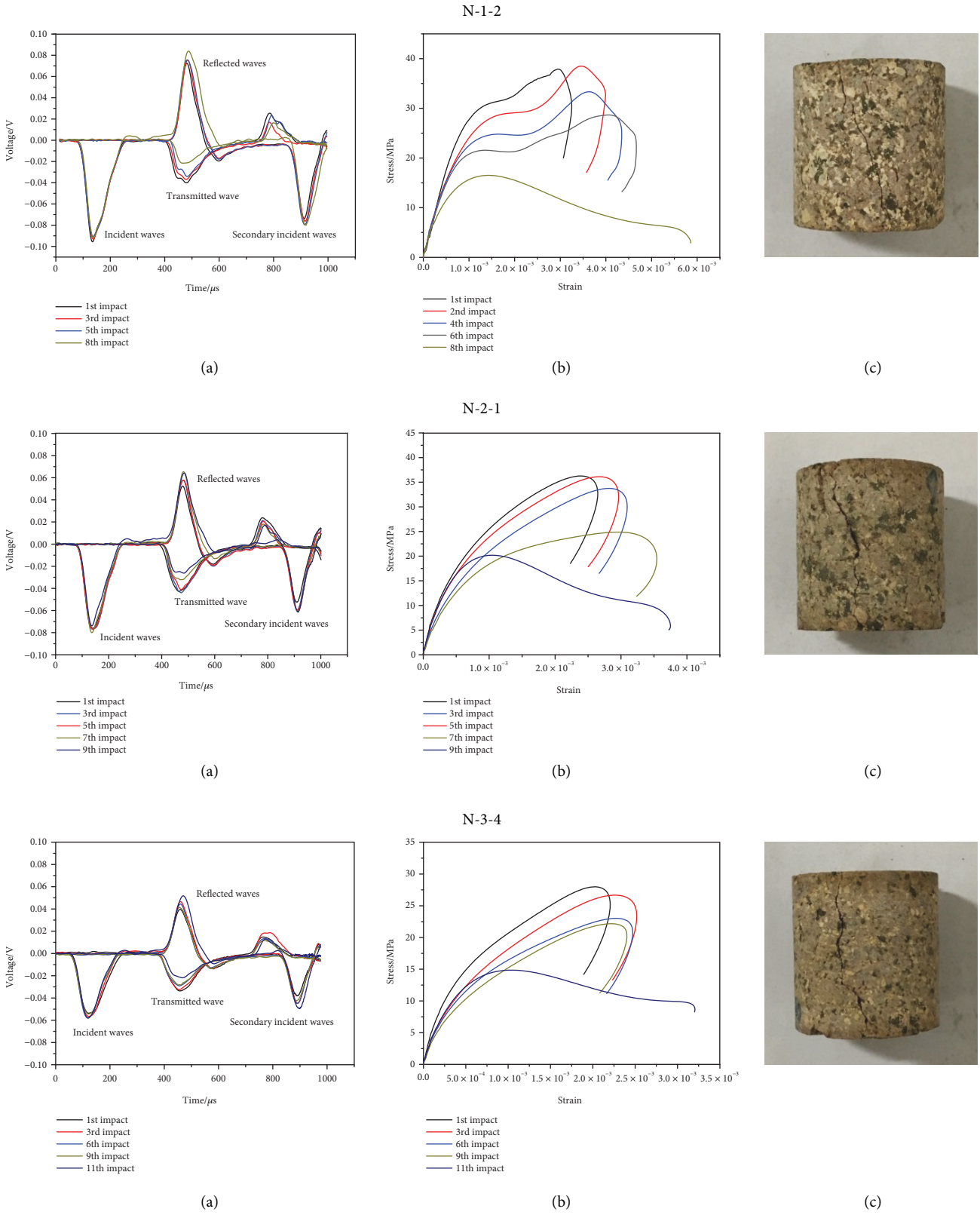


FIGURE 8: Dynamic response of weakly weathered granites under cyclic impacts of approximately constant velocity: (a) strain signal waveform, (b) stress-strain curve, and (c) failure modes.

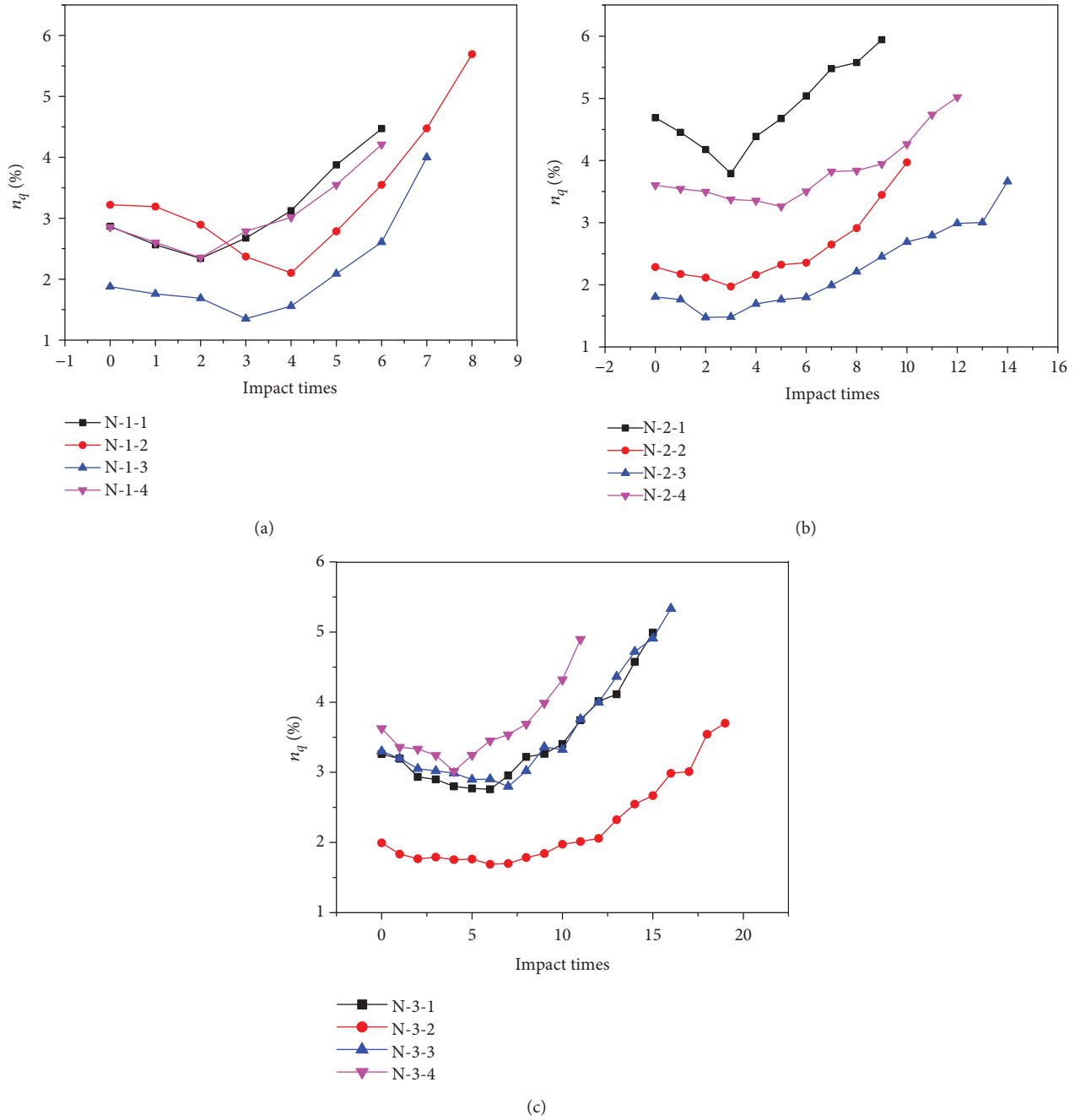


FIGURE 9: The relationship between effective porosity and impact times.

which was the same as the failure curve of samples under single impacts. This indicated that during this process, the samples were suddenly damaged and not induced by gradually accumulated damage.

From the NMR T_2 spectrum and Figure 11, the compaction process can be found in the first two impacts. Pores in the rocks showed a positive correlation with transverse relaxation time of fluids in pores [40]. T_2 spectrum distribution of weakly weathered granite samples before and after impacts maintained three peak values. Pores in the samples were roughly divided into three types, i.e., small, medium, and large pores according to their sizes, corresponding to three wave peaks in T_2 spectrum (from left to right). After

each impact, the distribution of the T_2 spectrum changed, indicating that the proportion of pores of each size dynamically changed with influences of cyclic impact disturbances. These multiscale changes were found, involving the constant generation of new micropores and the development and extension of initial micropores to medium- and large-sized pores. After the third and fourth impacts, large and medium pores changed most significantly [10]. The overall shape of the T_2 spectrum shifted to the right, and NMR signals of large pores were enhanced. This showed that with the increase in impact times, small pores were developed to medium- and large-sized pores until macroscopic damage occurred [41].

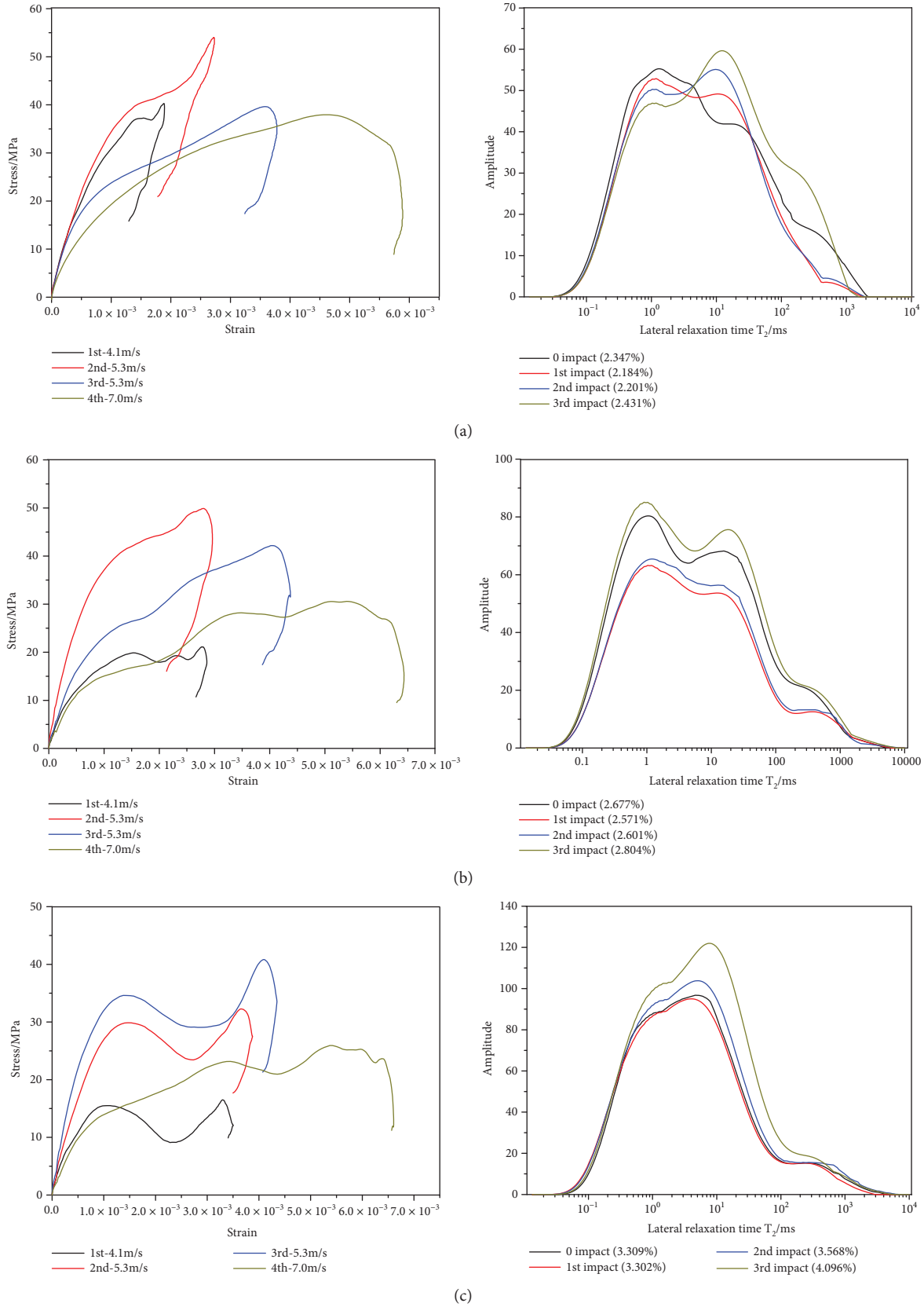


FIGURE 10: Stress-strain curve and T_2 spectrum of weakly weathered granites.

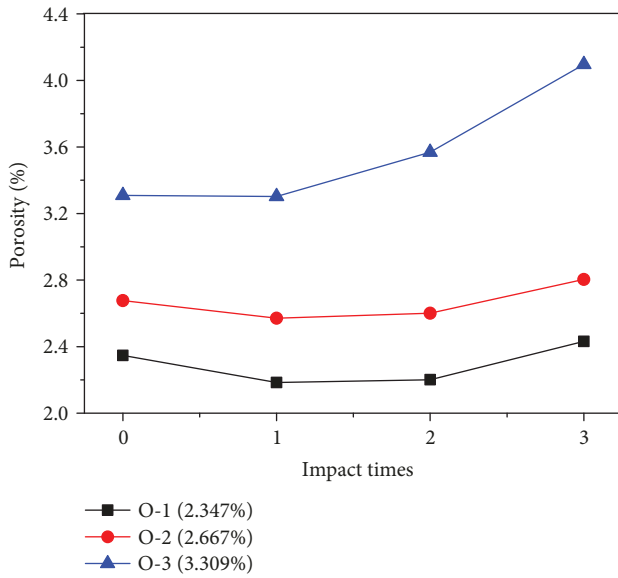


FIGURE 11: The relationship between effective porosity and impact times.

As demonstrated in Figure 11, the larger the initial porosity, the higher the degree of concentration of microcracks in the samples. Under the disturbance of cyclic impacts, cracks in the samples with a large porosity extended and connected at a faster rate and to a larger degree. This demonstrated that the growth rate of porosity and porosity before damage were relatively large. Also, the compaction process gradually weakened until it disappeared with an increase in initial porosity of the samples.

3.4. Relationship between Pore Change and Permeability Coefficient. In Section 3.1, only one unconnected crack was generated in the samples with an impact velocity of approximately 7 m/s, which could not reach the ideal permeability enhancement effects. In Section 3.2, many impact times were required to generate macroscopic damage and the compaction process was relatively long during which damage to the surrounding rocks accumulated and overall stability of ore bodies reduced. Using the scheme of cyclic impacts with increasing velocity, the impact times in the compaction process could be effectively reduced, avoiding accumulation of damage. After the third impact, porosity was larger than the initial porosity. After the fourth impact, the samples were damaged and the bearing capacity had significantly decreased, which could not meet the requirements for stability. In the test, it was reasonable to carry out variable-speed cyclic impacts in triplicate, which was better than the constant-speed cyclic impacts in practice. However, whether the permeability changes after three impacts met the requirements of permeability enhancement should be considered.

The triaxial seepage tests were conducted on the samples in the O group before impacts and after three variable-speed cyclic impacts. Figure 12 shows the changes of porosity and permeability coefficients of some samples in the O group

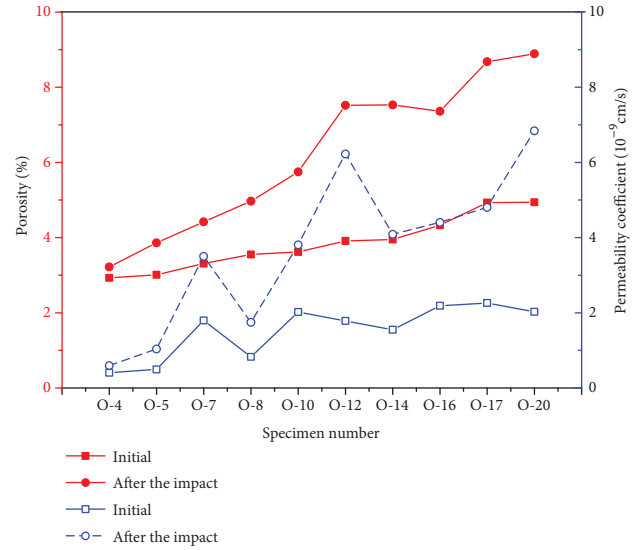


FIGURE 12: Change of porosity and permeability coefficient before and after impact of weakly weathered granite.

before and after three impacts. The samples were numbered according to porosity from small to large.

As displayed in Figure 12, the increment in porosity after cyclic impacts increased with initial porosity, which corresponded to Section 3.3. The initial permeability coefficient was positively correlated with porosity [19], but this relationship was not always true. This demonstrated that the porosity of rocks affected permeability, and the permeability coefficient depended on the number of seepage channels formed by internal defects in rocks and the content of clay minerals [18, 42, 43]. After cyclic impacts, the permeability coefficient increased and the increment rose with the increment in porosity. However, it did not always follow this law. When the permeability coefficient was firstly determined, the connected seepage channels were formed under the pore water pressures in rocks. After the first impact, the seepage channels in the samples were compacted or extended, and new microcracks were formed. In general, the volume of compacted cracks was larger than that of the extending and generated microcracks. In the last two impacts, crack expansion and connection were mainly shown in the samples to form new seepage channels. The weathering degrees of different weakly weathered granite samples had small differences which are reflected by the content of internal clay minerals. Moreover, the clays could be found on the fractures of the damaged samples. Owing to the presence of clays blocking seepage channels, the permeability of mine seams was reduced, showing that the permeability coefficient of some samples with large porosity was smaller than that of the samples with small porosity. The structure and distribution of initial defects in the rocks determined the damage degree after cyclic impacts affecting the permeability coefficient. The test results showed that after three impacts, the effects of the above factors on permeability coefficient could be avoided. This forms sufficient seepage channels, achieving the goal of enhancing permeability of ore bodies.

4. Conclusions

This study conducted uniaxial, constant-speed cyclic, and variable-speed cyclic impact compression tests on weakly weathered granites using an improved SHPB device. By combining with NM-60 NMR analysis and GDS-VIS triaxial seepage test, the research analyzed the pore evolution of rocks and changes of permeability coefficient. This provides theoretical references and test methods for blasting-induced permeability enhancement processes. Based on the summarization and analysis of the test results, the following conclusions can be made:

- (1) Under single impacts of weakly weathered granites, the cyclic impact velocity that could generate effective damage ranged from 4 to 7 m/s. There was a critical strain value from the damage of rocks to macroscopic failure. When the peak strain was larger than 0.005, rocks were damaged
- (2) Under variable-speed cyclic impacts, with a decrease in impact velocity, the cyclic times of impact to cause fracture increased, whilst the amplitudes of dynamic peak strength and strain signal waveforms were reduced. With increasing cyclic times of impact loading, the deformation modulus decreased, whilst the dynamic peak strength firstly increased and then decreased. Moreover, peak strain was the smallest when rock failure occurred under the impact. Rock failure resulted from the accumulation of damages which was a progressive process. The porosity showed an initial decrease and then increase with increasing impact times
- (3) Under variable-speed cyclic impacts, both dynamic peak strength and deformation modulus firstly increased and then decreased. There were three scales of pores in weakly weathered granites and small pores extended to medium-sized and then large-sized pores under cyclic impacts. After four impacts on the samples, the larger the initial porosity, the weaker the compaction process which also disappeared. After the third impact, the porosity was the largest
- (4) After the variable-speed cyclic impacts had been repeated three times on weakly weathered granites, the influences of content of clay minerals, weathering degree, initial pore structure, and distribution on permeability coefficient could be avoided. As a result, the permeability coefficient increased, achieving the goal of blasting-induced permeability enhancement, whilst the relationship of increasing permeability coefficient with an increase in porosity is not applicable to all cases

In addition, this study conducted laboratory tests of blasting-induced permeability enhancement on ion-adsorbed rare earth ores in granite weathering crust. The design of blasting parameters needs to be further determined by combining these data with outdoor similarity tests in the future.

Data Availability

The data used to support the findings of this study are included within the article.

Conflicts of Interest

The authors declare no conflict of interest regarding the publication of this paper.

Acknowledgments

The work was supported by a project funded by the National Natural Science Foundation of China (51404111 and 51604127), the China Scholarship Council (201708360023), a project funded by the China Postdoctoral Science Foundation (2014M562529XB), a Scientific Research Project of Jiangxi Provincial Education Department (GJJ160643), and the Programme of Qingjiang Excellent Young Talents, Jiangxi University of Science and Technology, China. The aforementioned financial supports are much appreciated.

References

- [1] A. X. Wu, H. J. Wang, B. H. Yang, and S. H. Yin, "Progress and prospect of leaching mining technology prospect of leaching mining technology," *Mining Technology*, vol. 6, no. 3, pp. 39–48, 2006.
- [2] Y. X. Li, L. Zhang, and X. M. Zhou, "Resource and environment protected exploitation model for ion-type rare earth deposit in southern of China," *Chinese Rare Earths*, vol. 31, no. 2, pp. 80–85, 2010.
- [3] Z. B. Huang, X. Cai, X. Q. Yuan, and Q. Wang, "Simple analysis for safety problems in the in-situ leaching mining of ionic rare earth mine," *Chinese Rare Earths*, vol. 34, no. 4, pp. 99–102, 2013.
- [4] Y. S. Ding, L. Chen, X. Xie et al., "On the stimulation with 'exploding in fractures' in low permeability reservoirs," *Petroleum Exploration and Development*, vol. 28, no. 2, pp. 90–96, 2001.
- [5] Y. S. Zhao, D. Yang, Y. Q. Hu, Z. C. Feng, and L. Zhao, "Study on the effective technology way for mining methane in low permeability coal seam," *Journal of China Coal Society*, vol. 6, no. 5, pp. 455–458, 2001.
- [6] T. Ren and F. T. Wang, "Gas reservoir simulation for enhanced gas recovery with nitrogen injection in low permeability coal seams," *International Journal of Oil, Gas and Coal Technology*, vol. 10, no. 3, pp. 272–292, 2015.
- [7] F. Wang, C. Zhang, and N. Liang, "Gas permeability evolution mechanism and comprehensive gas drainage technology for thin coal seam mining," *Energies*, vol. 10, no. 9, p. 1382, 2017.
- [8] W. Wei, L. Xiao-Chun, Y. Wei, W. Qizhi, and L. Guifeng, "Model test and mechanism study of the blasting-enhanced permeability of sandstone-type uranium deposits of low-permeability," *Chinese Journal of Rock Mechanics and Engineering*, vol. 35, no. 8, pp. 1609–1617, 2016.
- [9] Q. B. Zhang and J. Zhao, "A review of dynamic experimental techniques and mechanical behaviour of rock materials," *Rock Mechanics and Rock Engineering*, vol. 47, no. 4, pp. 1411–1478, 2014.

- [10] K. Zhou, B. Li, J. L. Li, H. W. Deng, and F. Bin, "Microscopic damage and dynamic mechanical properties of rock under freeze-thaw environment," *Transactions of Nonferrous Metals Society of China*, vol. 25, no. 4, pp. 1254–1261, 2015.
- [11] K. Xia, M. H. B. Nasser, B. Mohanty, F. Lu, R. Chen, and S. N. Luo, "Effects of microstructures on dynamic compression of Barre granite," *International Journal of Rock Mechanics and Mining Sciences*, vol. 45, no. 6, pp. 879–887, 2008.
- [12] W. Wang, H. Wang, D. Li, H. Li, and Z. Liu, "Strength and failure characteristics of natural and water-saturated coal specimens under static and dynamic loads," *Shock and Vibration*, vol. 2018, Article ID 3526121, 15 pages, 2018.
- [13] W. Wang, H. M. Li, R. P. Yuan, and H. L. Gu, "Micromechanics analysis and mechanical characteristics of water-saturated coal samples under coupled static-dynamic loads," *Journal of China Coal Society*, vol. 41, no. 3, pp. 613–619, 2016.
- [14] F. Q. Gong, X. B. Li, and X. L. Liu, "Preliminary experimental study of characteristics of rock subjected to 3D coupled static and dynamic loads," *Chinese Journal of Rock Mechanics and Engineering*, vol. 30, no. 6, pp. 1179–1190, 2011.
- [15] F. Q. Gong, X. B. Li, X. L. Liu, and J. Zhao, "Experimental study of dynamic characteristics of sandstone under one-dimensional coupled static and dynamic loads," *Chinese Journal of Rock Mechanics and Engineering*, vol. 29, no. 10, pp. 2076–2085, 2010.
- [16] X. B. Li, T. S. Lok, and J. Zhao, "Dynamic characteristics of granite subjected to intermediate loading rate," *Rock Mechanics and Rock Engineering*, vol. 38, no. 1, pp. 21–39, 2005.
- [17] J. J. Zhu, X. B. Li, F. Q. Gong, and S. Wang, "Dynamic characteristics and damage model for rock under uniaxial cyclic impact compressive loads," *Chinese Journal of Geotechnical Engineering*, vol. 35, no. 3, pp. 531–539, 2013.
- [18] X. Liu, M. Xu, and K. Wang, "Mechanism of permeability evolution for reservoir sandstone with different physical properties," *Geofluids*, vol. 2018, Article ID 5327895, 16 pages, 2018.
- [19] J. Tian, R. A. Chi, G. C. Zhu, S. M. Xu, X. Qiu, and Z. G. Zhang, "Leaching hydrodynamics of weathered elution-deposited rare earth ore," *Transactions of Nonferrous Metals Society of China*, vol. 11, no. 3, pp. 434–437, 2001.
- [20] X. Li, Z. Zhou, T. S. Lok, L. Hong, and T. Yin, "Innovative testing technique of rock subjected to coupled static and dynamic loads," *International Journal of Rock Mechanics and Mining Sciences*, vol. 45, no. 5, pp. 739–748, 2008.
- [21] F. Dai, S. Huang, K. Xia, and Z. Tan, "Some fundamental issues in dynamic compression and tension tests of rocks using split Hopkinson pressure bar," *Rock Mechanics and Rock Engineering*, vol. 43, no. 6, pp. 657–666, 2010.
- [22] Y. X. Zhou, K. Xia, X. B. Li et al., "Suggested methods for determining the dynamic strength parameters and mode-I fracture toughness of rock materials," *International Journal of Rock Mechanics and Mining Sciences*, vol. 49, no. 1, pp. 105–112, 2012.
- [23] L. Yan, L. Liu, S. Zhang, D. Lan, and J. Liu, "Testing of weakly weathered granites of different porosities using a split Hopkinson pressure bar technique," *Advances in Civil Engineering*, vol. 2018, Article ID 5267610, 11 pages, 2018.
- [24] X. Lishi, "Recent development on nuclear magnetic resonance in rock samples and its application," *Well Logging Technology*, vol. 29, no. 1, pp. 27–31, 1996.
- [25] K. P. Zhou, J. L. Li, Y. J. Xu, and Y. M. Zhang, "Measurement of rock pore structure based on NMR technology," *Journal of Central South University*, vol. 43, no. 12, pp. 4796–4800, 2012.
- [26] X. B. Li, T. S. Lok, J. Zhao, and P. J. Zhao, "Oscillation elimination in the Hopkinson bar apparatus and resultant complete dynamic stress-strain curves for rocks," *International Journal of Rock Mechanics and Mining Sciences*, vol. 37, no. 7, pp. 1055–1060, 2000.
- [27] X. B. Li, Z. L. Zhou, D. S. Liu, Y. Zou, and T. Yin, "Wave shaping by special shaped striker in SHPB tests," in *Advances in rock dynamics and applications*, pp. 105–123, CRC Press, Taylor & Francis Group, Boca Raton, 2011.
- [28] X. Li, Y. Zou, and Z. Zhou, "Numerical simulation of the rock SHPB test with a special shape striker based on the discrete element method," *Rock Mechanics and Rock Engineering*, vol. 47, no. 5, pp. 1693–1709, 2014.
- [29] Z. Zhou, X. Li, A. Liu, and Y. Zou, "Stress uniformity of split Hopkinson pressure bar under half-sine wave loads," *International Journal of Rock Mechanics and Mining Sciences*, vol. 48, no. 4, pp. 697–701, 2011.
- [30] D. Mohr, G. Gary, and B. Lundberg, "Evaluation of stress-strain curve estimates in dynamic experiments," *International Journal of Impact Engineering*, vol. 37, no. 2, pp. 161–169, 2010.
- [31] L. Song and S. Hu, "Two-wave and three-wave method in SHPB data processing," *Explosion and Shock Waves*, vol. 25, no. 4, pp. 368–373, 2005.
- [32] W. A. Wei, X. U. Wei-ya, and W. A. Ru-bin, "Permeability of dense rock under triaxial compression," *Chinese Journal of Rock Mechanics and Engineering*, vol. 34, no. 1, pp. 40–47, 2015.
- [33] T. Yin, L. Bai, X. Li, X. Li, and S. Zhang, "Effect of thermal treatment on the mode I fracture toughness of granite under dynamic and static coupling load," *Engineering Fracture Mechanics*, vol. 199, pp. 143–158, 2018.
- [34] Y. M. Yang, Y. Ju, H. B. Liu, and H. J. Wang, "Influence of porous structure properties on mechanical performances of rock," *Chinese Journal of Rock Mechanics and Engineering*, vol. 28, no. 10, pp. 2031–2038, 2009.
- [35] Y. Ju, Y. M. Yang, Y. Z. Mao, H. B. Liu, and H. J. Wang, "Laboratory investigation on mechanisms of stress wave propagations in porous media," *Science in China Series E: Technological Sciences*, vol. 52, no. 5, pp. 1374–1389, 2009.
- [36] Y. Zou, J. Li, L. He, L. Laloui, and J. Zhao, "Wave propagation in the vicinities of rock fractures under obliquely incident wave," *Rock Mechanics and Rock Engineering*, vol. 49, no. 5, pp. 1789–1802, 2016.
- [37] H. P. Xie, Y. Ju, and L. Y. Li, "Criteria for strength and structural failure of rocks based on energy dissipation and energy release principles," *Chinese Journal of Rock Mechanics and Engineering*, vol. 24, no. 17, pp. 3003–3010, 2005.
- [38] H. Deng, C. J. Chuan, K. Bo, Y. Wang, and Y. N. Zhang, "Experimental study on microscopic damage characteristics of granite under cyclic dynamic disturbances," *Chinese Journal of Engineering*, vol. 39, no. 11, 1639 pages, 2017.
- [39] L. L. Wang, *Foundation of Stress Waves*, National Defense Industry Press, Beijing, China, 2005.
- [40] O. Mohnke, "Jointly deriving NMR surface relaxivity and pore size distributions by NMR relaxation experiments on partially desaturated rocks," *Water Resources Research*, vol. 50, no. 6, pp. 5309–5321, 2014.

- [41] J. L. Li, K. P. Zhou, W. J. Liu, and H. Deng, "NMR research on deterioration characteristics of microscopic structure of sandstones in freeze-thaw cycles," *Transactions of Nonferrous Metals Society of China*, vol. 26, no. 11, pp. 2997–3003, 2016.
- [42] C. L. Zhang, "The stress-strain-permeability behaviour of clay rock during damage and recompaction," *Journal of Rock Mechanics and Geotechnical Engineering*, vol. 8, no. 1, pp. 16–26, 2016.
- [43] D. Xiao, S. Jiang, D. Thul, S. Lu, L. Zhang, and B. Li, "Impacts of clay on pore structure, storage and percolation of tight sandstones from the Songliao Basin, China: implications for genetic classification of tight sandstone reservoirs," *Fuel*, vol. 211, pp. 390–404, 2018.



Hindawi

Submit your manuscripts at
www.hindawi.com

